SCA2003-10

STATISTICAL SYNTHESIS OF IMAGE ANALYSIS AND MERCURY POROSIMETRY FOR MULTISCALE PORE STRUCTURE CHARACTERIZATION

E. Amirtharaj, M.A. Ioannidis and I.F. Macdonald

Department of Chemical Engineering, University of Waterloo,
Waterloo, Ontario N2L 3G1, Canada

ABSTRACT

A novel method is developed for determining the continuous distribution of pore sizes in reservoir rock over the range 0.01-1000 μm. The method employs a statistical description of the microstructure to combine information from mercury intrusion porosimetry (MIP) and image analysis. Central to this method is the observation that the pore size distribution obeys a fractal scaling law over a range of sizes accessible by both MIP and imaging methods ($.01 < r < 10$ μm). For a number of sandstone and carbonate samples it is verified that the surface fractal dimension obtained by analysis of MIP data is consistent with that obtained by image analysis. Data fusion is achieved in Fourier space. Accordingly, the scattering intensity data computed in the size range $1 < r < 1000$ μm from the measured two-point correlation function are extrapolated in the range $.01 < r < 1$ μm using the known fractal scaling law. The extended scattering intensity data are interpreted using a model of scattering from a distribution of spherical pores. The resulting pore size distribution is used to compute a synthetic drainage capillary pressure curve, comparison of which to the MIP data furnishes new information on the pore-to-throat aspect ratio and pore accessibility.

INTRODUCTION

The pore structure of sedimentary rock is a chaotic network of interconnected pores, the sizes of which can range from nanometers to millimeters. The rock-pore interface is known to have extensive fractal properties [1], but fractal scaling laws cannot describe the microstructure over all length scales. In the absence of great diagenetic alteration, a considerable fraction of the pore volume can in fact be explained by Euclidean models based on grain packing and compaction [2]. The presence of angular pores in such models does not eliminate the need to account for the entire spectrum of pore length scales when capillary properties of reservoir rock are of interest. This is evident in attempts to predict the amount of capillary-bound water [3] or to explain the rate and extent of spontaneous imbibition [4]. Similarly, estimation of electrical resistivity and relative permeability at low values of water saturation fails if pore geometry is not adequately resolved over sub-micrometric length scales [5], *i.e.*, well within the size range where fractal scaling laws apply [6, 7].

An experimentally validated picture of sedimentary rock, honoring length scales of the order of the grain size as well as length scales associated with microporosity, is exceptionally difficult to obtain. Although numerous experimental probes of pore geometry are available (*e.g.*, gas adsorption, small-angle scattering, mercury porosimetry, petrographic image analysis, nuclear magnetic resonance relaxometry and imaging, X-ray microtomography, *etc.*), no method can probe five or more orders of magnitude of the pore length scale, as required. Direct imaging methods, such as backscatter scanning electron microscopy (BSEM) [8] and X-ray microtomography [9] become unwieldy for providing statistically significant microstructure data at length scales smaller than about 1 micrometer. These methods are not well suited for the study of the surface fractal characteristics of sedimentary rocks. Indirect imaging methods, like small-angle neutron and X-ray scattering (SANS and SAXS), yield the volume-averaged Fourier transform of the density correlation function on length scales ranging from one nanometer to about 10 micrometers [1]. Greater length scales, accounting for much of the pore volume in sedimentary rock, cannot be probed by these techniques. Mercury intrusion porosimetry (MIP) may be used to invasively probe the pore space in the range 20 nm to 100 μm. This method does not provide the pore size distribution, but rather the distribution of pore volume accessible to mercury through pore throats (volumeless constrictions in the pore space) of different size. Lack of information on the distribution, spatial clustering and interconnectedness of pore bodies makes the interpretation of MIP data extremely complex, if not impossible [10]. Analysis of the NMR relaxation properties of fluid-saturated samples may also be used to estimate the pore size distribution [11]. The results of such analysis, however, can be distorted by diffusional averaging of magnetization between pores [12] and rendered ambiguous by uncertainty of the surface relaxivity value.

Recently, Radlinski *et al*. [13] obtained the entire distribution of pore length scales in a sample of reservoir sandstone by combining small-angle scattering and BSEM imaging data within a statistical framework. The same computational framework is used in the present work, except that MIP and not SANS is employed to access structural information in the sub-micrometric range.

THEORETICAL FRAMEWORK

The most general description of a porous medium is in terms of a statistical phase function $Z(\mathbf{x})$, taking the value of unity if **x** points to solid and zero otherwise. The first two moments of $Z(\mathbf{x})$ are the porosity, $\phi = \langle Z(\mathbf{x}) \rangle$ and the two-point correlation function, $S_2(\mathbf{r}) = \langle Z(\mathbf{x}) Z(\mathbf{x}+\mathbf{r}) \rangle$, where **r** is a lag vector and angular brackets denote statistical averages. For isotropic media the two-point correlation function depends only on the modulus of the lag vector, i.e. $S_2(\mathbf{r}) = S_2(r)$. For length scales greater than about 1 μm, the function $S_2(r)$ is readily determined by statistical analysis of binary micrographs of the pore space [8]. In small-angle scattering (SAS) experiments, the

scattering intensity is the Fourier transform of the density-density correlation function $\gamma(r)$:

$$I(Q) = \frac{d\sigma}{d\Omega}(Q) = 4\pi \int_0^\infty r^2 \gamma(r) \frac{\sin(Qr)}{Qr} dr \tag{1}$$

where $\gamma(r) = (\Delta\rho)^2 \phi(1-\phi) R_z(r)$, $R_Z(r) \equiv (S_2(r) - \phi^2)/(\phi - \phi^2)$ is the void-void autocorrelation function and $Q = 2\pi/r$. For neutron scattering in sedimentary rocks, regardless of their organic matter content, the scattering length density contrast, $(\Delta\rho)^2$, between various rock components is small compared to the contrast between any of these components and the void [1]. Therefore, rocks scatter neutrons as a quasi-two-phase system. Consequently, the function $I(Q)$ measured by SANS and the function $S_2(r)$ calculated from BSEM images are a Fourier transform pair. It is on this basis that SANS and BSEM imaging information are combined to obtain the scattering cross section $I(Q)$ in the range $10^{-7} < Q < 10^{-1}$ Å^{-1} [13]. Inverse Fourier transform then yields the autocorrelation $R_z(r)$ in the size range 10 Å < r < 1 mm:

$$R_Z(r) = \frac{1}{2\pi^2 (\Delta\rho)^2 \phi(1-\phi)} \int_0^\infty Q^2 I(Q) \frac{\sin(Qr)}{Qr} dQ \tag{2}$$

Clearly, if $S_2(r)$ is experimentally available from BSEM images over a range of r-values, $I(Q)$ can be calculated in the corresponding Q-range using Eq. (1). The $I(Q)$ data computed in this manner are limited to relatively small Q-values, since the resolution of BSEM data is typically of the order of 1 μm.

For a surface fractal object of dimension D, the scattering intensity follows the power law $I(Q) \propto Q^{D-6}$ with $2 < D < 3$. This scaling holds in the large Q-range, but breaks down for length scales of the order of tens of micrometers, *i.e.*, for length scales of the order of grain size. The range of pore length scales over which a fractal scaling law applies (large Q-range) may also be accessed by MIP. Indeed, this technique has been used to determine surface fractal dimensions [14], yielding results in agreement with SAXS measurements [15]. Fractal analysis of MIP data is based on the scaling law:

$$-dS_{Hg}/dr \propto r^{2-D} \tag{3}$$

where $S_{Hg}(r)$ is the sample saturation to mercury at capillary pressure $P_C \propto 1/r$. Eq. (3) is consistent with a scaling of the number-based pore size distribution according to the power law $f(r) \propto r^{-(D+1)}$.

Over a limited range of pore length scales, $I(Q)$ data computed from $S_2(r)$ via Eq. (1) also follow the scaling $I(Q) \propto Q^{D-6}$, thus providing an estimate of D that can be compared to the one obtained by analysis of MIP data using Eq. (3). Provided that correspondence between the two values is established, one may extrapolate $I(Q)$ in the large Q-range according to $I(Q) \propto Q^{D-6}$. Thus, structural information about pore length scales not probed by BSEM may be accounted for quantitatively and consistently.

To obtain the complete distribution of pore length scales from the extended $I(Q)$ data, we assume that the solid-void interface has a locally spherical geometry. According to this assumption the scattering intensity per unit volume is given by [13]:

$$I(Q) = (\Delta\rho)^2 \frac{\phi}{\langle V_r \rangle} \int_{R_{\min}}^{R_{\max}} V_r^2 f(r) F_s(Qr) dr \tag{4}$$

In Eq. (4), $R_{\max}$ and $R_{\min}$ are the maximum and minimum pore radii, respectively, $V_r \equiv V(r) = (4/3)\pi r^3$ is the volume of a sphere of radius r, $\langle V_r \rangle = \int_{R_{\min}}^{R_{\max}} V_r f(r) dr$ is the average pore volume, $f(r)$ is the probability density of the pore size distribution, and $F_s(Qr)$ is the form factor for a sphere of radius r:

$$F_s(Qr) = \left[3 \frac{\sin(Qr) - Qr\cos(Qr)}{(Qr)^3} \right]^2 \tag{5}$$

The function $f(r)$ is determined by inversion of the extended $I(Q)$ data using Eq. (4). The cumulative distribution of pore volume is then computed from $f(r)$ and plotted along the MIP data as a function of equivalent capillary pressure for purposes of comparison.

RESULTS AND DISCUSSION

The rock samples studied include Berea sandstone, several Middle Silurian dolomite samples with variable amounts of vuggy porosity, obtained from three boreholes in Cambridge, Ontario, and several sandstone samples from the Late Cretaceous Chatsworth formation (Ventura County, Southern California). Core analysis measurements (porosity by a saturation method, Klinkenberg-corrected permeability, formation factor and cementation exponent) are provided in Table 1. Also included are key image analysis results, such as image resolution, porosity and integral correlation length, Λ. The latter parameter corresponds to a characteristic pore length scale and is determined from the void-void autocorrelation function as follows:

$$\Lambda = \int_0^{\infty} R_Z(r) dr \tag{6}$$

The length scale Λ has been previously shown to explain permeability variations in reservoir rock [8]. Porosimetry tests (injection and withdrawal) were performed on 1-cm^3 cubic samples lightly coated with epoxy on all but one faces to minimize surface penetration effects. MIP-measured porosity is also given in Table as are estimates of the average pore surface-to-volume ratio, *s*, obtained by MIP and image analysis. The following comments are in order:

Table 1. Summary of petrophysical and image analysis[1] measurements.

Code	Lithology[2]	k (mD)	ϕ	F	m	Resolution (μm/pixel)	ϕ_{img}	Λ (μm)	s_{img} (μm^{-1})	D_{img}	ϕ_{MIP}	s_{MIP} (μm^{-1})	D_{MIP}
Berea	Ss	660	0.202	35	2.22	2.0	0.214	25.0	0.406	2.52	0.220	9.34	2.58
16Ap4	dol	31	0.116	188	2.43	2.0	0.111	42.4	0.241	2.58	0.091	17.98	2.61
16Ap5	dol	45	0.100	131	2.15	3.4	0.103	60.8	0.123	2.57	0.085	3.97	2.68
16Bp7	dol, vg	55	0.100	162	2.21	2.0	0.126	63.2	0.251	2.60	0.082	11.80	2.63
16Bp11	dol, vg	1.7	0.110	102	2.10	1.25	0.088	7.6	1.404	2.93	0.082	15.79	2.88
16Bp17	dol, vg	1200	0.160	161	2.17	7.0	0.194	115.2	0.106	2.77	0.066	39.7	2.88
16Bp18	dol	250	0.167	55	2.14	2.7	0.175	53.5	0.268	2.71	0.162	7.36	2.66
16Bp19	dol, vg	20	0.090	189	2.21	3.2	0.092	74.0	0.155	2.89	0.055	31.05	2.89
13P5	dol, vg	12	0.122	92	2.15	1.3	0.146	17.1	1.228	-	0.083	5.10	2.52
13P7	dol, vg	0.76	0.088	102	1.99	0.5	0.106	4.6	2.093	-	0.066	12.12	2.95
13P11	dol, vg	2.3	0.078	184	2.04	1.1	0.100	15.9	1.14	2.70	0.068	16.47	2.69
13P20	dol, vg	904	0.140	71	2.17	2.7	0.160	74.6	0.172	2.68	0.103	6.46	2.64
C3-408	ss, slt	2.5	0.121	73	2.03	2.7	0.100	19.9	0.625	2.71	0.112	22.06	2.60
C4-207	ss, slt	6.4	0.158	58	2.20	1.3	0.134	10.9	0.988	2.60	0.107	4.67	2.32
C4-137	ss, slt	12.1	0.171	39	2.07	2.0	0.173	19.3	0.561	2.76	0.125	6.91	2.64
C6-495	ss, slt	11.7	0.137	37	1.82	3.4	0.099	28.5	0.321	2.73	0.113	23.99	2.66
C6-174	ss, slt	18.5	0.151	57	2.14	2.5	0.162	26.2	0.434	2.68	0.124	6.31	2.40
C6-271	ss, slt	1.4	0.104	120	2.12	3.7	0.077	28.8	0.530	2.90	0.094	31.76	2.61

[1]A minimum of 15 images (1022 × 768 pixels) per sample were analyzed. [2]ss = sandstone, dol = dolomite, vg = vuggy, slt = silty.

(i) Core analysis, BSEM and MIP investigate different rock volumes. Porosity estimates by each of these methods will not coincide, unless the rock is fairly homogeneous.

(ii) MIP probes pore length scales much smaller than are accessible by BSEM. Consequently, the pore surface-to-volume ratio measured by image analysis is, in general, an order of magnitude smaller than that measured by MIP.

(iii) Estimates of the surface fractal dimension, D, by MIP and image analysis agree reasonably well for the majority of the samples studied. These values indicate that the rock-pore interface is, in all cases, quite rough.

(iv) As seen in Fig. 1, the permeability of the media studied is estimated with good engineering accuracy from the empirical equation of Ioannidis *et al*. [8]. This result is remarkable considering the variability of the rock samples studied, and provides further support for the relevance of the length scale Λ to permeability.

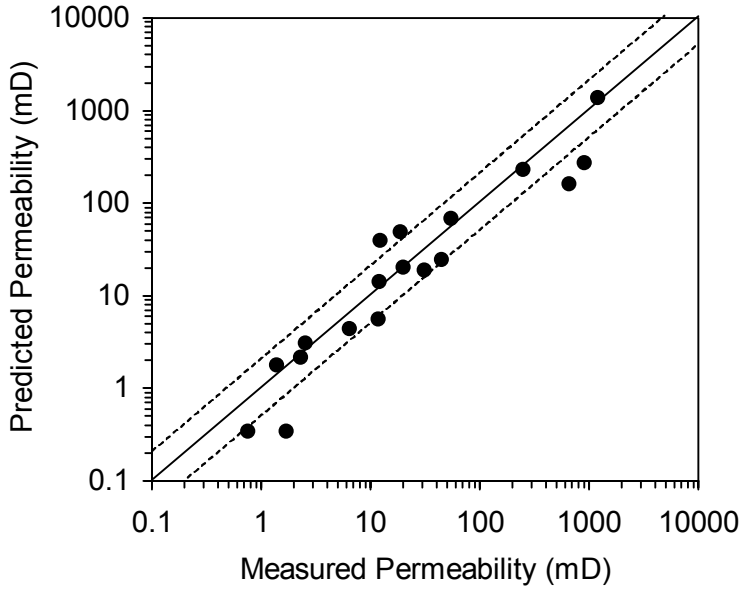

Figure 1. Permeability prediction from image analysis data (ϕ, Λ). Dotted lines correspond to error of a factor of two.

The new method of multiscale pore structure characterization is first illustrated in Fig. 2 for the Berea sandstone sample. The estimation of surface fractal dimension D = 2.58 from MIP data via Eq. (3) is shown in Fig. 2(a). The $I(Q)$ data computed from the image-derived $R_Z(r)$ via Eq. (1) show fractal scaling consistent with the MIP findings, and are extrapolated in the large-Q range using $I(Q) \propto Q^{D-6}$ with D = 2.58, as illustrated in Fig. 2(b). Inversion of the extended $I(Q)$ data according to Eq. (4) produces the pore size distribution shown in Fig. 2(c). The cumulative pore volume distribution (PVD), calculated from the $f(r)$, is compared to the respective MIP data in Fig. 3 and Fig. 4, for representative sandstone and carbonate samples. To facilitate comparison of the two sets

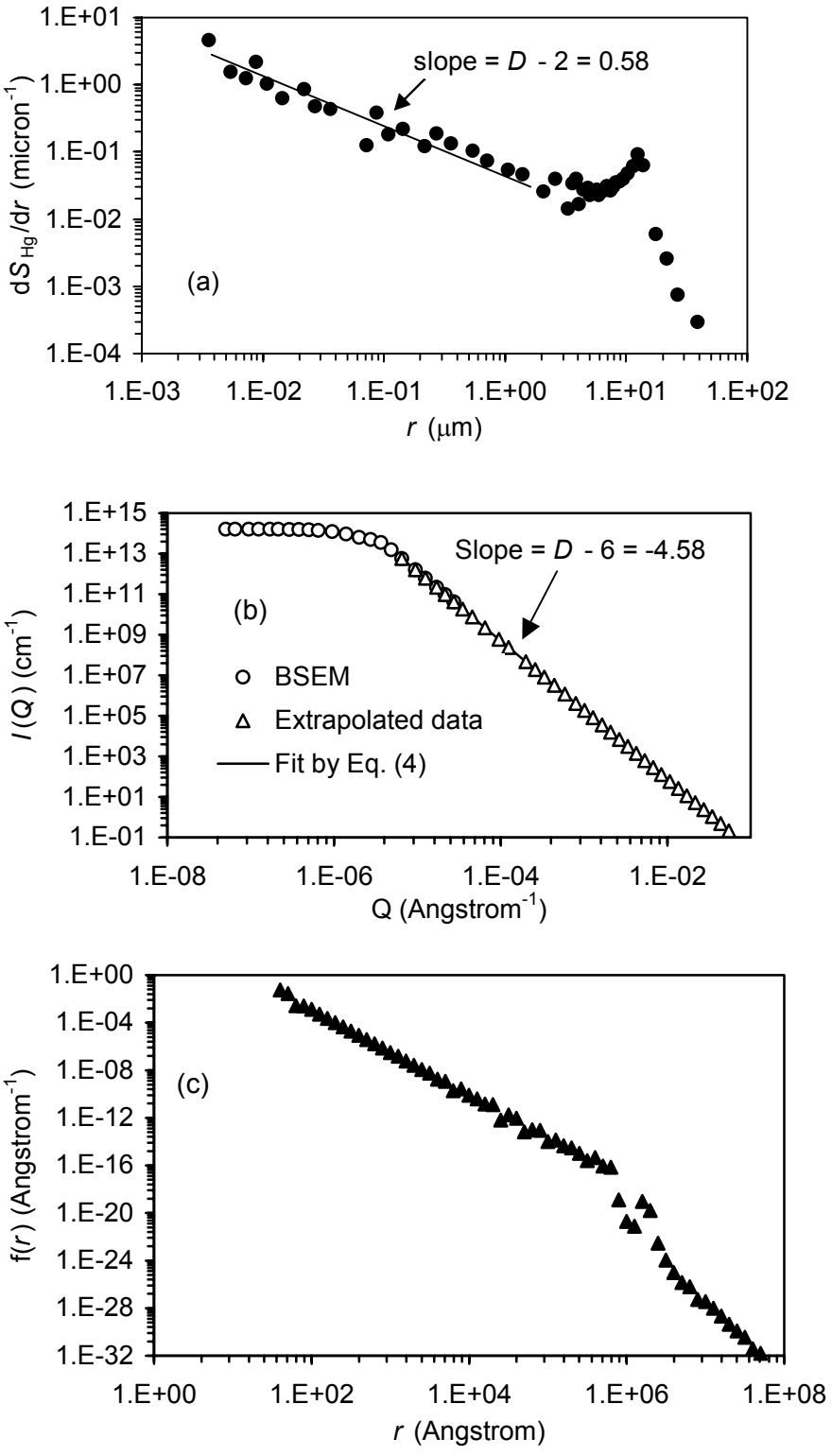

Figure 2. Statistical fusion of MIP and BSEM microstructure data (see text for details).

(a) Sample: Berea

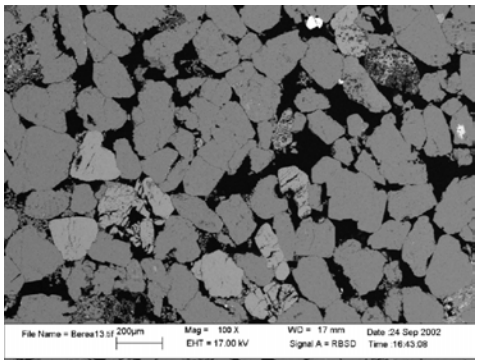

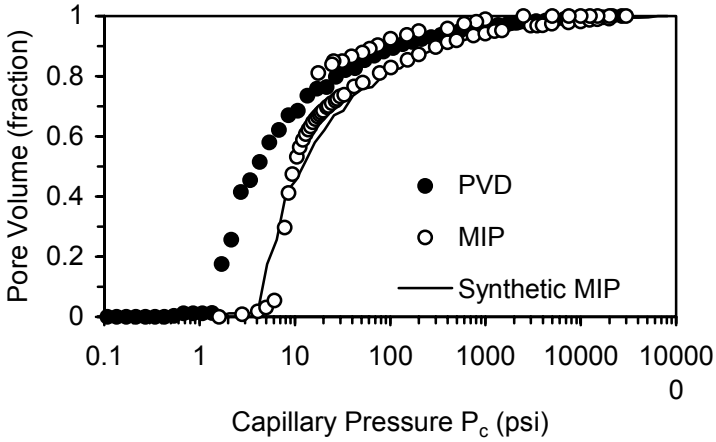

(b) Sample: C6-495

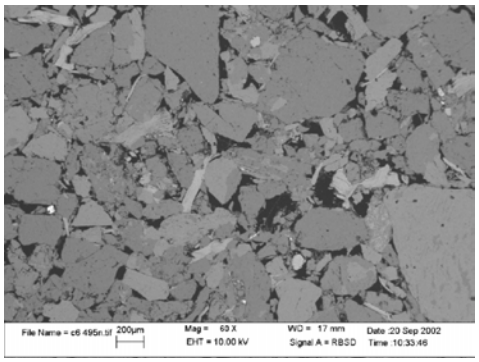

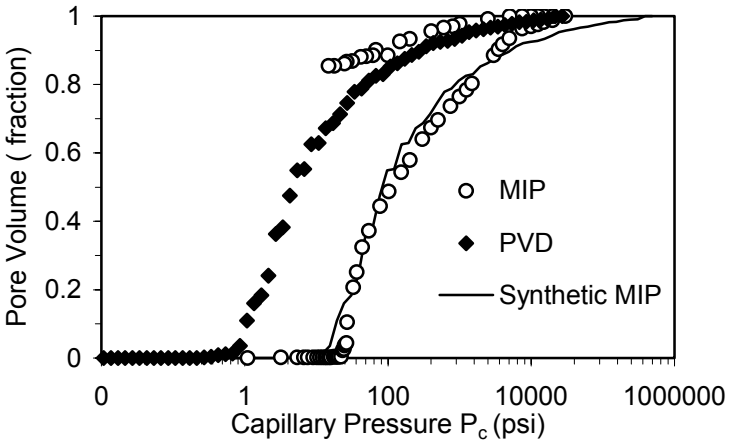

(c) Sample: C3-408

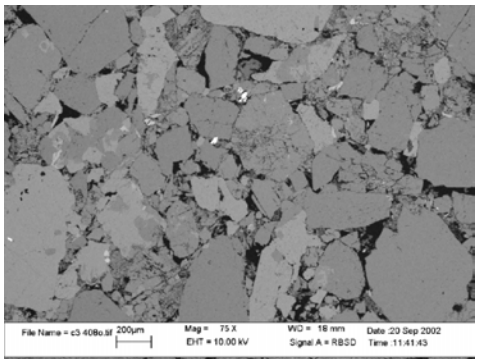

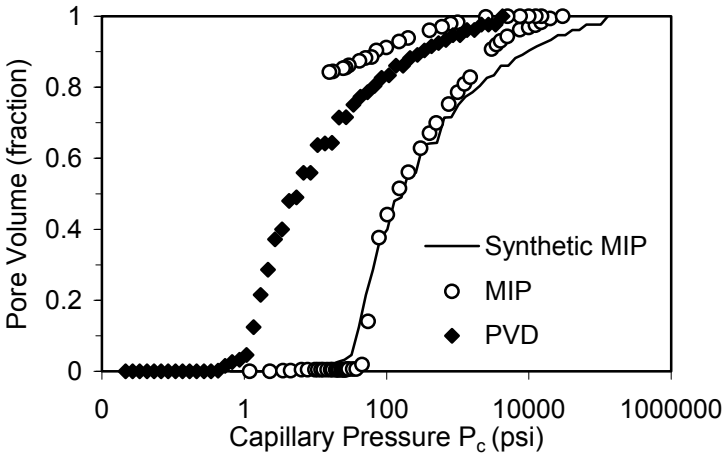

Figure 3. Distribution of pore volume by pore size (PVD), distribution of accessible pore volume by pore throat size (MIP) and simulated MIP result assuming complete pore accessibility and constant pore-to-throat aspect ratio of: (a) 3, (b) 18, (c) 30.

(a) Sample: 16Ap4

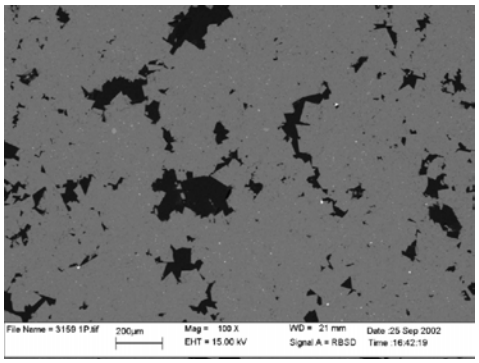

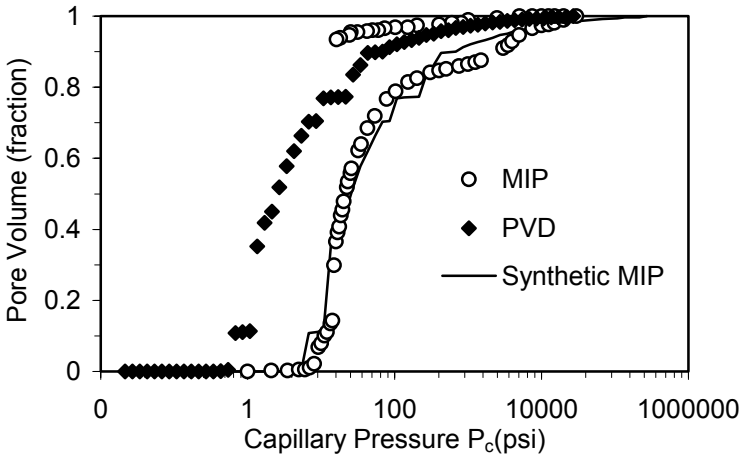

(b) Sample: 16Bp18

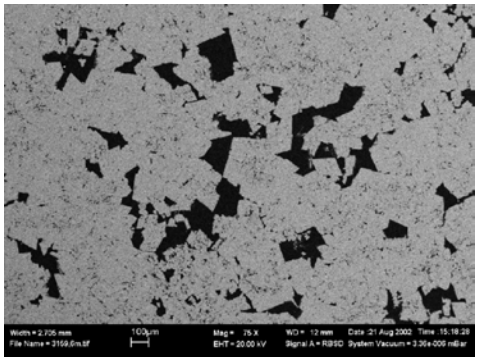

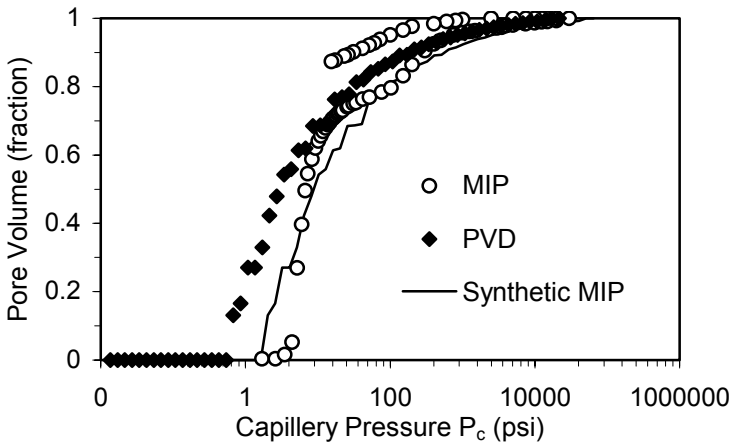

(c) Sample: 13P20

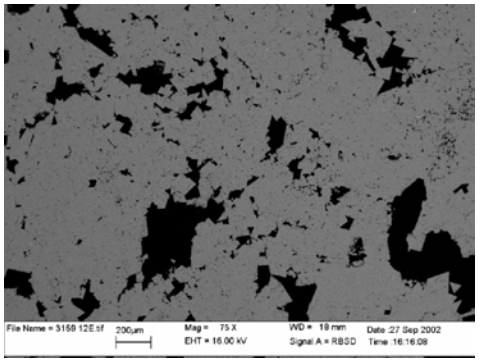

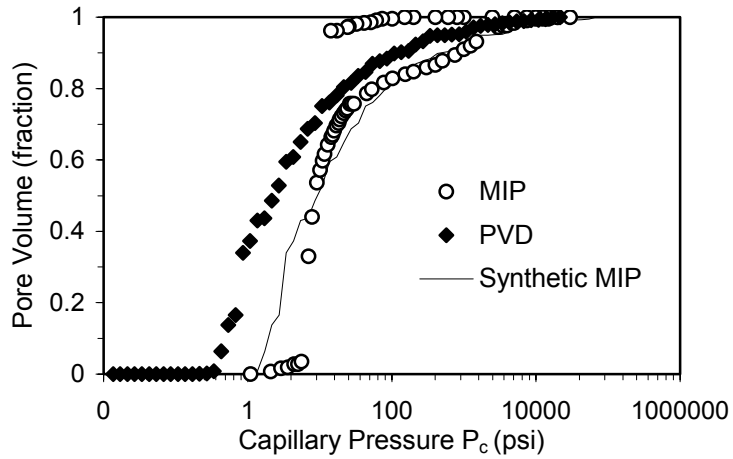

Figure 4. Distribution of pore volume by pore size (PVD), distribution of accessible pore volume by pore throat size (MIP) and simulated MIP result assuming complete pore accessibility and constant pore-to-throat aspect ratio: (a) 10, (b) 3, (c) 4.

of data, pore radius r is converted to capillary pressure using $P_C = 2\sigma\cos\theta/r$. The comparison may be discussed as follows.

The PVD curve spans five orders of magnitude of the length scale. This curve lies always to the left of the MIP data. This is a consequence of the fact that the length scale controlling P_C in the MIP experiment corresponds to the size of local constrictions in the pore space (pore throats), and does not reflect the size of pore bodies. The two curves might be made to overlap if two conditions were satisfied: (a) the pore-to-throat size aspect ratio is known and, (b) each pore is invaded by mercury at a value of the capillary pressure corresponding to the size of the pore throat through which the pore is invaded. The latter condition corresponds to complete pore accessibility to the non-wetting phase. The extent to which the above conditions are met may be tested by assuming a constant pore-to-throat aspect ratio, r_p / r_t and examining the degree of overlap between the shifted PVD and MIP curves.

As shown in Fig. 3(a) for the Berea sandstone sample, the value $r_p / r_t \approx 3$ brings the two curves into coincidence over the entire range of pore sizes. Song [16] has obtained a similar result about the pore-to-throat aspect ratio in Berea sandstone, from an analysis of porosimetry and NMR data. A similar value has been found by Radlinski *et al*. [13] for a different sample of well-sorted, relatively clay-free sandstone. By contrast, the comparison of shifted PVD and MIP curves for poorly-sorted, clayey sandstone samples yields much greater aspect ratios (see also [16]), as shown in Fig. 3(b) and Fig. 3(c). These results reveal in a quantitative manner what may be suspected by careful inspection of the micrographs. Namely, in clean, well-sorted samples small pore throats do not control access of the non-wetting phase to large pores, whereas the opposite is true for the poorly-sorted, clayey samples. Note that large pores (of comparable size) are present in both Berea sandstone and the poorly-sorted, less permeable samples shown in Fig. 3. The pore length scale Λ of these media is, in fact, quite similar (see Table 1). For the carbonate samples the PVD curves demonstrate bimodal features, in qualitative agreement with MIP results (see Fig. 4). The comparison between the PVD and MIP curves yields values of r_p / r_t in the range $1 < r_p / r_t < 20$. For these media, however, the same value of r_p / r_t cannot, in general, bring the two curves into coincidence over the entire range of pore sizes. This result is not surprising considering the complex pore geometries encountered in vuggy carbonates (see Fig. 4). In view of the enormous variability of pore length scales present, the following picture of sandstone pore structure emerges. This picture corresponds to a multiscale (hiearchical) percolation network. In well-sorted, relatively clay-free sandstones, pores of similar size form percolating networks at all scales. In poorly-sorted, clayey sandstones, the networks of largest pores do not percolate. These pores are instead invaded by the nonwetting phase at capillary pressures corresponding to fluid percolation into pore networks at a smaller scale.

An attractive feature of the pore structure characterization method pursued in this work is the determination of pore size distribution over all length scales that can be probed by

image analysis and mercury porosimetry. These are broadly accessible techniques of pore structure characterization, lending the method suitable for routine petrophysical evaluation. Both fractal and Euclidean aspects of pore geometry are represented. This results in a continuous pore size distribution, which can be compared to MIP results offering novel insight into the accessibility of pores of different size to a non-wetting phase. This comparison provides information on the relationship between an *apparent* pore-to-throat aspect ratio and pore size, examples of which are given in Fig. 5. Such information is useful for assessing the potential for non-wetting phase entrapment in pores of different sizes. Independent knowledge of the pore size distribution is also essential for the correct interpretation of mercury porosimetry and NMR relaxation data using network models of the pore structure [10, 12] and may be directly incorporated into models of relative permeability [7].

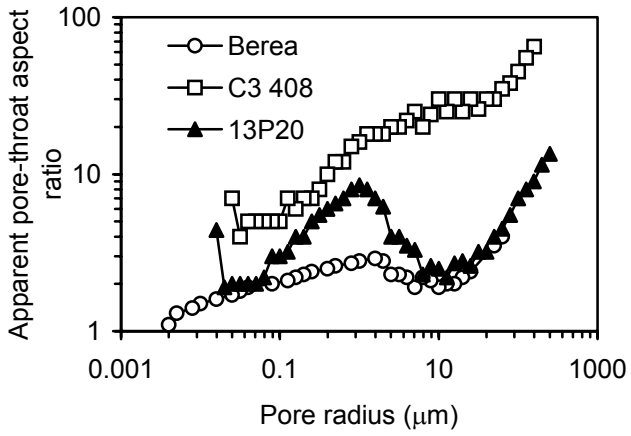

Figure 5. Apparent pore-to-throat aspect ratio in different samples.

CONCLUSIONS

Fractal measures of pore structure, accessible by mercury porosimetry (MIP), are combined with BSEM image data within a statistical framework. Assuming that the pore space has a locally spherical geometry, the continuous distribution of pore size is derived in the range 0.01 μm to 1000 μm for a suite of sandstone and carbonate rock samples. Novel information on the pore-to-throat aspect ratio and pore accessibility is obtained by comparing the complete pore volume distribution (PVD) to the MIP data.

REFERENCES

1. Radlinski, A.P., Radlinska, E.Z., Agamalian, M., Wignall, G.D., Lindner, P., and Randl, O.G., "Fractal geometry of rocks", Physical Review Letters, (1999) 82, 3078-3081.
2. Bryant, S., Cade, C., and Mellor, D., "Permeability prediction from geologic models", American Association of Petroleum Geologists Bulletin, (1993) 77, 1338-1350.

3. Song, Y.Q., Ryu, S.G., and Sen, P.N., "Determining multiple length scales in rocks", Nature, (2000) 406, 178-181.
4. Constantinides, G.N., and Payatakes, A.C., "Effects of precursor wetting films in immiscible displacement through porous media", Transport in Porous Media, (2000) 38, 291-317.
5. Bekri, S., Howard, J., Muller, J., and Adler, P.M., "Electrical resistivity in multiphase flow through porous media", Transport in Porous Media, (2003) 51, 1, 46-72.
6. Tsakiroglou, C.D., and Fleury, M., "Pore network analysis of resistivity index for water-wet porous media", Transport in Porous Media, (1999) 35, 89-128.
7. Vizika, O., and Kalaydjian, F., "Effect of capillary, viscous and gravity forces on gas condensate mobility", Paper SCA2002-24, Annual Symposium of the Society of Core Analysts, Monterey, California, Sept. 23-27, 2002.
8. Ioannidis, M.A., Kwiecien, M.J., and Chatzis, I., "Statistical analysis of the porous microstructure as a method for estimating reservoir permeability", Journal of Petroleum Science and Engineering, (1996) 16, 251-261.
9. Spanne, P., Thovert, J.-F., Jacquin, C., Lindquist, W., Jones, K., and Adler, P., "Synchrotron computed microtomography of porous media: topology and transports", Physical Review Letters, (1994) 73, 2001-2004.
10. Tsakiroglou, C.D., and Payatakes, A.C., " Characterization of the pore structure of reservoir rocks with the aid of serial sectioning analysis, mercury porosimetry and network simulation", Advances in Water Resources, (2000) 23, 773-789.
11. Dunn, K.J., Bergman, D.J., and LaTorraca, G.A., *Nuclear Magnetic Resonance Petrophysical and Logging Applications*, Handbook of Geophysical Exploration, vol. 32, Helbig, K. and Treitel, S. (eds.), Pergamon, Amsterdam, 2002.
12. Chang, D., and Ioannidis, M.A., "Magnetization evolution in network models of porous rock under conditions of drainage and imbibition", Journal of Colloid and Interface science, (2002) 253, 159-170.
13. Radlinski, A.P., Ioannidis, M.A., Hinde, A.L., Hainbuchner, M., Baron, M., Rauch, H., and Kline, S.R., "Multiscale characterization of reservoir rock microstructure: Combining small-angle neutron scattering and image analysis", Paper SCA2002-35, Annual Symposium of the Society of Core Analysts, Monterey, California, Sept. 23-27, 2002.
14. Ehrburger-Dolle, F., Lavanchy, A., and Stoeckli, F., "Determination of the surface fractal dimension of active carbons by mercury porosimetry", Journal of Colloid and Interface Science, (1994) 166, 451-461.
15. Blacher, S., Heinrichs, B., Sahouli, B., Pirard, J., and Pirard, J.-P., "Fractal characterization of wide pore range catalysts: Application to Pd-Ag/SiO_2 xerogels", Journal of Colloid and Interface Science, (2000) 226, 123-130.
16. Song, Y.Q., "Pore sizes and pore connectivity in rocks using the effect of internal field", Magnetic Resonance Imaging, (2001) 19, 417-421.